

Seasonal Cycle of the Mixed Layer Heat Budget in the Northeastern Tropical Atlantic Ocean

GREGORY R. FOLTZ, CLAUDIA SCHMID, AND RICK LUMPKIN

NOAA/Atlantic Oceanographic and Meteorological Laboratory, Miami, Florida

(Manuscript received 12 January 2013, in final form 2 May 2013)

ABSTRACT

The seasonal cycle of the mixed layer heat budget in the northeastern tropical Atlantic (0° – 25° N, 18° – 28° W) is quantified using in situ and satellite measurements together with atmospheric reanalysis products. This region is characterized by pronounced latitudinal movements of the intertropical convergence zone (ITCZ) and strong meridional variations of the terms in the heat budget. Three distinct regimes within the northeastern tropical Atlantic are identified. The trade wind region (15° – 25° N) experiences a strong annual cycle of mixed layer heat content that is driven by approximately out-of-phase annual cycles of surface shortwave radiation (SWR), which peaks in boreal summer, and evaporative cooling, which reaches a minimum in boreal summer. The surface heat-flux-induced changes in the mixed layer heat content are damped by a strong annual cycle of cooling from vertical turbulent mixing, estimated from the residual in the heat balance. In the ITCZ core region (3° – 8° N) a weak seasonal cycle of mixed layer heat content is driven by a semiannual cycle of SWR and damped by evaporative cooling and vertical turbulent mixing. On the equator the seasonal cycle of mixed layer heat content is balanced by an annual cycle of SWR that reaches a maximum in October and a semiannual cycle of turbulent mixing that cools the mixed layer most strongly during May–July and November. These results emphasize the importance of the surface heat flux and vertical turbulent mixing for the seasonal cycle of mixed layer heat content in the northeastern tropical Atlantic.

1. Introduction

Sea surface temperature (SST) in the tropical Atlantic is characterized by a strong seasonal cycle that projects onto longer time scale climate fluctuations (Chiang et al. 2002; Bates 2010; Doi et al. 2010; Foltz et al. 2012). Pronounced seasonality is evident in the two main modes of interannual–decadal variability in the tropical Atlantic: the meridional mode (Nobre and Shukla 1996; Chang et al. 1997; Chiang and Vimont 2004) and the Niño mode (Zebiak 1993; Keenlyside and Latif 2007). On average, the meridional mode is about 50% stronger in April compared to August (Chiang and Vimont 2004), and the Atlantic Niño mode tends to peak in July with an amplitude about 50% larger compared to its amplitude in February (Keenlyside and Latif 2007). The strong seasonality of each mode reflects the influence of the tropical Atlantic seasonal cycle (e.g., Carton and Huang 1994;

Chiang et al. 2002) and the seasonality of forcing from the equatorial Pacific and North Atlantic (e.g., Czaja et al. 2002).

The northeastern tropical Atlantic (NETA) (0° – 25° N, 18° – 28° W) in particular exhibits a strong seasonal cycle (Fig. 1; Carton and Zhou 1997) that is not completely understood. Part of the difficulty in understanding the seasonal cycle in the NETA stems from the strong latitudinal dependence of SST, surface winds, and cloudiness (Figs. 1a,e) associated with the intertropical convergence zone (ITCZ), combined with very few long-term observations in the NETA. Until the recent deployments of Argo floats (beginning in \sim 2001) and the Prediction and Research Moored Array in the Tropical Atlantic (PIRATA) Northeast Extension (beginning in 2006), the NETA was one of the most sparsely sampled regions of the tropical Atlantic Ocean. Coupled climate models have also been of limited use for understanding the seasonal cycle in the NETA because of large annual mean and seasonal biases in this region, especially close the equator (Muñoz et al. 2012; Doi et al. 2012).

Several studies have explored the mechanisms that drive seasonal variability in the NETA. In the latitude

Corresponding author address: Gregory Foltz, NOAA/Atlantic Oceanographic and Meteorological Laboratory, 4301 Rickenbacker Causeway, Miami, FL 33149.
E-mail: gregory.foltz@noaa.gov

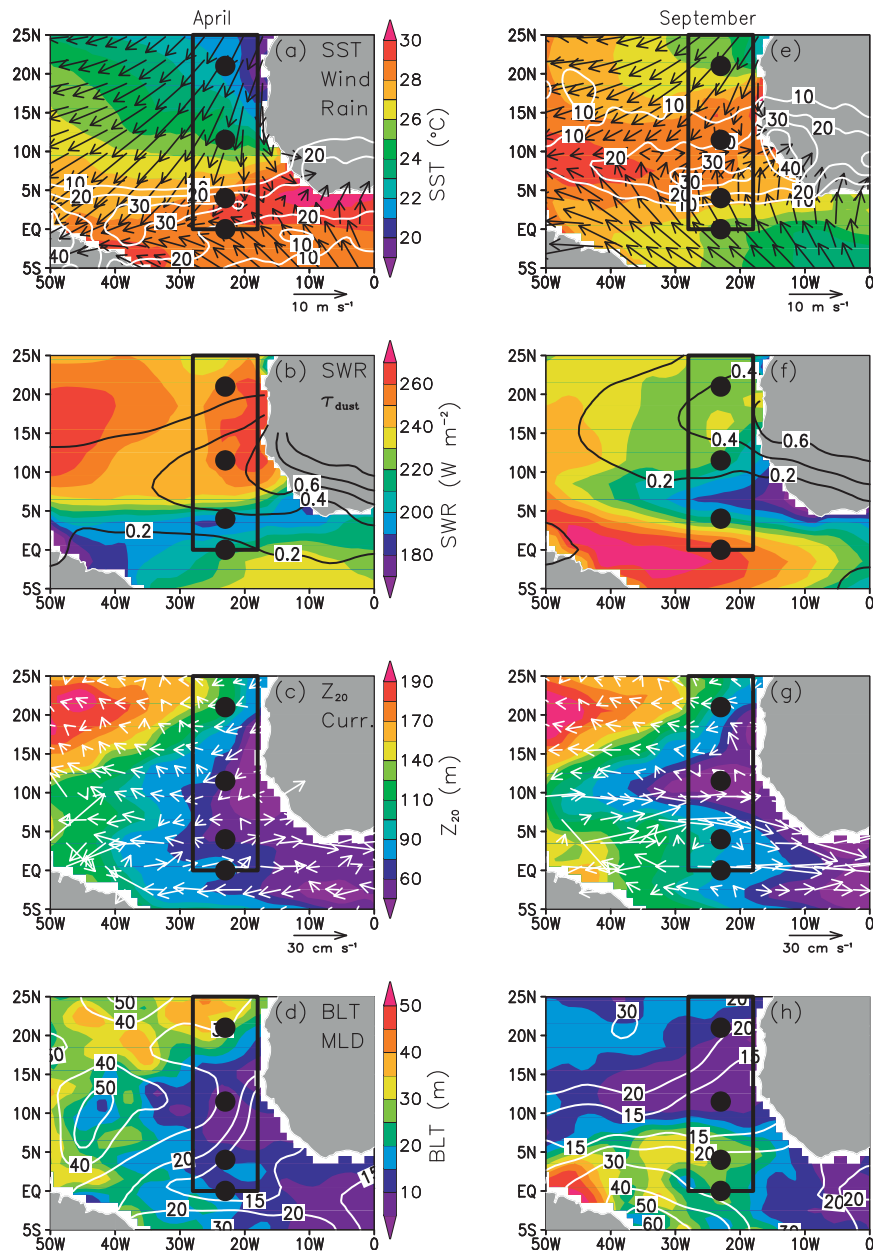


FIG. 1. April mean (2001–11) (a) SST (shaded), surface wind velocity (vectors), and precipitation (contours, cm). (b) Surface shortwave radiation (shaded) and dust aerosol optical thickness (contours). (c) Depth of the 20°C isotherm (shaded) and surface currents (vectors). (d) Barrier layer thickness (shaded) and mixed layer depth (contours). (e)–(h) As in (a)–(d), but for September. Black boxes show the northeastern tropical Atlantic region, which is the focus of this study, and black dots indicate the positions of the PIRATA moorings used in this study.

band of the ITCZ (2°–10°N), ocean–atmosphere coupling exerts a strong influence on the seasonal cycle. Meridional migrations of the ITCZ throughout the year have been attributed to positive coupling between SST, surface winds, evaporation, and upwelling (Mitchell and Wallace 1992; Xie and Philander 1994; Chang and Philander

1994). The establishment of a cold tongue of SST in the equatorial Atlantic during boreal spring and summer leads to an intensification of the southeasterly trade winds in the eastern equatorial Atlantic, which in turn generates stronger upwelling and cooler SST (e.g., Caniaux et al. 2011). The ITCZ moves northward with the band of

warmest SST, which is maintained against damping by weaker wind-induced evaporative cooling and upper-ocean mixing (Xie and Philander 1994).

Despite broad agreement that SST in the NETA plays an active role in shaping the seasonal cycle in the tropical Atlantic, the mechanisms that drive the seasonal cycle of SST in the NETA are not well understood. Carton and Zhou (1997) showed in a series of numerical ocean model experiments that the annual cycle of SST along the equator (2°S – 2°N) west of 20°W is driven by meridional Ekman divergence and associated upwelling. North of 10°N the annual cycle of solar radiation was found to dominate, except within a few degrees of the African coast where seasonal changes in coastal upwelling were found to be most important. Yu et al. (2006) used a combination of satellite, reanalysis, and in situ data to show that the seasonal cycle of SST is driven by the net surface heat flux poleward of 10°N and 5°S . In contrast to the results of Carton and Zhou (1997), Yu et al. (2006) found that coastal upwelling does not contribute significantly to the seasonal cycle of SST off the coast of northwest Africa. In the equatorial and ITCZ regions (5°S – 10°N) Yu et al. concluded that seasonal variations of Ekman divergence and associated upwelling contribute significantly to the seasonal cycle of SST.

Previous studies more focused on the equatorial Atlantic generally agree with the broader-scale analyses of Carton and Zhou (1997) and Yu et al. (2006). Foltz et al. (2003) found large seasonal cycles of zonal advection and vertical turbulent mixing in the mixed layer heat balance at 0° , 23°W with the strongest cooling from zonal advection occurring in boreal summer and from vertical mixing in boreal spring. Peter et al. (2006) found that the seasonal cycle of SST in the central equatorial Atlantic (18° – 23°W) is balanced by a warming tendency from the surface heat flux, with maxima in March and September, and a cooling tendency from vertical processes, which peaks during May–August and November–December. In contrast, between 4° and 8°N at 23°W seasonal variations of SST were found to be driven mainly by the surface heat flux, with a smaller contribution from cooling due to vertical processes that were strongest during February–April. On the equator between 18° and 23°W , Jouanno et al. (2011) showed two peaks in the cooling rate from vertical processes: one in May–June and another in November–December. They attributed the cooling primarily to vertical turbulent mixing driven by the shear between the eastward equatorial undercurrent and the westward south equatorial current. The cooling tendency during each period was partially balanced by warming from the surface heat flux.

Previous studies therefore generally agree that the seasonal cycle of SST in the NETA is driven primarily by

vertical turbulent mixing close to the equator and by the surface heat flux poleward of $\sim 10^{\circ}\text{N}$. There is no consensus on what drives the seasonal cycle of SST under the mean position of the ITCZ (2° – 10°N), where mean SSTs are high and ocean–atmosphere coupling is expected to be strong. In addition, most previous studies are based either on numerical modeling experiments or on statistical analyses of satellite and reanalysis datasets, each with its own limitations. Numerical models rely on parameterizations of vertical turbulent mixing and are affected by errors in surface forcing, while the statistical analyses of Yu et al. (2006) focused on the role of the net surface heat flux and did not explicitly consider the other terms in the heat balance (i.e., horizontal advection and vertical mixing). There is evidence of strong seasonal cycles of near-surface salinity stratification [i.e., the barrier layer, Tanguy et al. (2010) and Figs. 1d,h], near-surface currents [Stramma et al. (2005) and Figs. 1c,g], and SST gradients (Figs. 1a,e) in the NETA that may contribute significantly to the mixed layer heat budget through the horizontal advection and vertical mixing terms.

In this study, we analyze the mixed layer heat budget in the NETA using a combination of in situ, satellite, and reanalysis datasets, focusing on the period 2001–12, when high-quality measurements from Argo and the PIRATA Northeast Extension moorings are available. The emphasis is on latitudinal variations of the heat budget within the NETA and the processes that drive them, given the strong seasonal signal associated with the ITCZ and the meridional dependence of ocean–atmosphere coupling in the NETA.

2. Data

Data from several sources are used in this study. Vertical profiles of temperature and salinity in the upper 2000 dbar of the ocean were acquired from Argo floats during January 2001 through April 2012. These data include profiles that went through the scientific quality control developed for Argo (Owens and Wong 2009), as well as profiles that only went through the automatic quality control procedures applied by Argo Data Assembly Centers in real time. Mixed layer depth, barrier layer thickness, and depth of the 20°C isotherm (Z_{20}) were then computed from each profile using the methods described in the next section. The individual values of mixed layer depth, barrier layer thickness, and Z_{20} were then averaged to monthly means on a $1^{\circ} \times 1^{\circ}$ grid. Smoothing and gap filling in the gridded fields were then performed using optimum interpolation with a zonal scale of 300 km, meridional scale of 200 km, and time scale of 30 days. The monthly mean climatology in each grid box was used as the first guess for the interpolation.

Monthly mean surface heat fluxes were obtained from the TropFlux product (Kumar et al. 2012). The data are available on a $1^\circ \times 1^\circ$ grid for the period January 1979 through September 2011. Shortwave radiation (SWR) in TropFlux is calculated using the International Satellite Cloud Climatology Project (ISCCP) flux dataset (Zhang et al. 2004) climatology of SWR plus anomalies based on linear regression of ISCCP SWR onto satellite outgoing longwave radiation. The net surface longwave radiation (LWR) in TropFlux is from the European Centre for Medium-Range Weather Forecasts (ECMWF) Interim Re-Analysis (ERA-Interim). These data are not used in our analysis for reasons described in the following paragraph. We use the latent heat flux (LHF) and sensible heat flux (SHF) from TropFlux, which are computed using ERA-Interim wind speed and humidity together with satellite SST. All TropFlux fields were corrected for mean biases using data from tropical moored buoys.

Compared to the TropFlux LWR product, we found that the seasonal cycle of LWR from the National Centers for Environmental Prediction–National Center for Atmospheric Research (NCEP–NCAR) reanalysis (Kalnay et al. 1996) agrees better with direct measurements of LWR from PIRATA moorings along 23°W . We therefore use monthly mean LWR from the NCEP–NCAR reanalysis, which is available for 1948–present on a $2^\circ \times 2^\circ$ grid. We correct the NCEP–NCAR reanalysis LWR data for mean biases using direct measurements of LWR from PIRATA moorings (see section 3a). We also use daily mean wind speed at a height of 10 m and air temperature and specific humidity at a height of 2 m from the NCEP–NCAR reanalysis, after applying a seasonal bias correction, to fill gaps in the PIRATA air temperature, relative humidity, and wind speed time series. The methodology used to correct the NCEP–NCAR reanalysis meteorological parameters for seasonal biases is described in section 3b.

Monthly SWR, clear-sky SWR (clouds removed), “clean” sky SWR (aerosols removed), and clean clear-sky SWR (clouds and aerosols removed) are available from the Modern-Era Retrospective Analysis for Research and Applications (MERRA) on a $\frac{1}{2}^\circ$ latitude \times $\frac{2}{3}^\circ$ longitude grid for January 1979–present (Rienecker et al. 2011). These data are used to calculate the dependence of the seasonal cycle of SWR on the solar zenith angle, clouds, and aerosols. Monthly-mean aerosol optical thickness at 550 nm is available from the Moderate Resolution Imaging Spectroradiometer (MODIS) on board the *Aqua* and *Terra* satellites during February 2000–present on a $1^\circ \times 1^\circ$ grid. These data are converted to dust optical thickness (τ_{dust}) following Kaufman et al. (2005) and are used to illustrate seasonal variability of African dust in the NETA region (Figs. 1b,f).

We use monthly-mean chlorophyll-*a* concentration from the Sea-Viewing Wide Field-of-View Sensor (SeaWiFS) to estimate the amount of SWR absorbed in the mixed layer. These data are available on an 8-km grid during November 1997 through December 2010.

Daily mean SST and rainfall from the Tropical Rainfall Measuring Mission (TRMM)’s Microwave Imager (TMI) were obtained on a $\frac{1}{4}^\circ$ grid for the period January 1998–April 2012. Horizontal ocean velocity averaged in the upper 30 m is available from the Ocean Surface Current Analyses–Real Time (OSCAR) product during October 1992 to the present. Currents are calculated on a 1° grid using satellite altimetry, winds, and SST together with a diagnostic model (Bonjean and Lagerloef 2002). The TMI SST and OSCAR currents are used with the Argo mixed layer depth to calculate horizontal heat advection in the mixed layer (described in section 3a) after averaging the TMI SST and interpolating the Argo mixed layer depth to a 5-day resolution to match the resolution of the OSCAR product. Monthly mean climatological near-surface currents from drifting buoys on a $0.5^\circ \times 0.5^\circ$ grid (Lumpkin and Johnson 2013) are used with monthly TMI SST and Argo mixed layer depth for verification of the horizontal heat advection estimates based on OSCAR.

We obtained surface winds from the Quick Scatterometer (QuikSCAT) satellite for the period August 1999–November 2009. These data are available on a 0.5° grid from the Centre ERS d’Archivage et de Traitement (CERSAT) and are used to estimate wind-induced mixing at the base of the mixed layer. For consistency, we have resampled all datasets described in this section onto a $1^\circ \times 1^\circ$ grid. We limit our analysis of these data to January 2001–September 2010, when all data are available.

To complement the satellite-based and reanalysis products described above, direct measurements of subsurface temperature, salinity, horizontal velocity, and several meteorological parameters are available from PIRATA moorings (Bourlès et al. 2008) during September 1997–present. Here we use data from moorings at 0° , 4° , 11.5° , and 20.5°N along 23°W for the period January 1999–April 2012 (Fig. 1). All moorings measure temperature between 1 (i.e., SST) and 120 m at intervals of 3–20 m (Fig. 2). Salinity is measured at 6–8 levels between 1 and 120 m, and horizontal velocity is measured at a depth of 10 m. The mooring on the equator additionally measured horizontal velocity between 15 and 120 m from upward-looking acoustic Doppler current profilers (ADCP) during 2002, 2005–06, and 2008–09. All moorings measure wind velocity, relative humidity, air temperature, and SWR at heights 3–4 m above the sea surface. The moorings at 11.5°N

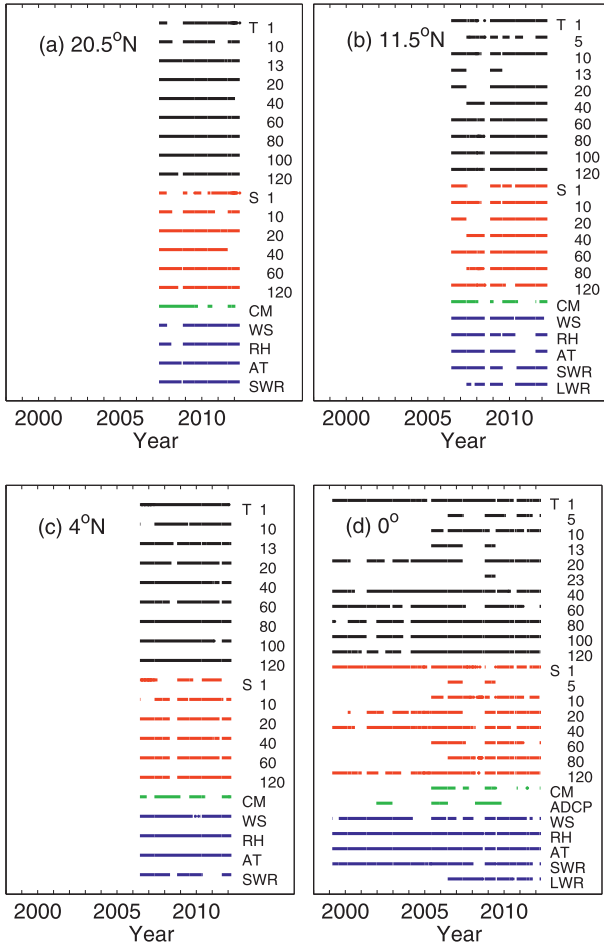


FIG. 2. Availability of daily measurements from the PIRATA moorings at (a) 20.5°N, (b) 11.5°N, (c) 4°N, and (d) 0° along 23°W. Black and red lines show subsurface temperature (T) and salinity (S), respectively, at the indicated depths. Green lines show current meter (CM) measurements at a depth of 20 m at all locations and vertical profiles of horizontal currents from ADCPs at 0°. Blue lines represent wind speed (WS), relative humidity (RH), air temperature (AT), SWR, and LWR.

and on the equator additionally measure downwelling longwave radiation.

We use daily averages of all PIRATA data, which are transmitted to shore in real time. The data records on the equator are the longest and exceed 13 years for some parameters (Fig. 2). The buoys at 4° and 11.5°N were initially deployed in 2006, and their records are therefore limited to 5–6 years. The buoy at 20.5°N has records of 4–5 years in length since it was deployed in 2007. Given the dominance of the seasonal cycle in the NETA and daily sampling from the moorings, four years is sufficient to produce a robust seasonal cycle for most parameters.

3. Methodology

To determine the processes responsible for the seasonal cycle of SST in the NETA, we analyze the heat budget in the surface mixed layer:

$$\rho c_p h \frac{\partial T}{\partial t} = -\rho c_p h \mathbf{v} \cdot \nabla T + Q_0 + \epsilon. \quad (1)$$

This formulation follows Kraus and Turner (1967) and Moisan and Niiler (1998). Changes in heat storage (left-hand term) are expressed in terms of horizontal heat advection (first term on the right), the net surface heat flux adjusted for the amount of SWR that penetrates the base of the mixed layer (second term on the right), and the residual ϵ , which is the combination of errors in the first three terms, vertical processes such as turbulent mixing, and other much smaller terms such as horizontal diffusion and the integral of the vertical temperature–velocity covariance (e.g., Hayes et al. 1991). Here h is the mixed layer depth, and T and \mathbf{v} are vertically averaged temperature and horizontal velocity in the mixed layer, respectively. Note that the heat storage rate in (1) includes only the term proportional to the rate of change of the mixed layer temperature and not the term proportional to the change in mixed layer depth. This formulation is chosen because we are interested in the processes that determine the seasonal cycle of SST, which is nearly identical to T , and not mixed layer heat storage (i.e., hT). The main advantage of using the heat budget formulation in (1), as opposed to the temperature budget in which (1) is divided by $\rho c_p h$, is that the residual of the heat balance is more easily interpreted in terms of physical processes since it is not weighted by h^{-1} .

Two complementary analyses of the heat balance in (1) are performed: one uses data from Argo, atmospheric reanalyses, and satellite-based analyses, and the other is based primarily on measurements from the PIRATA moorings. The first analysis provides the large-scale context and covers a longer time period (2001–10) compared to most PIRATA time series. The second analysis based on PIRATA is performed at four specific locations. The advantage is that the moorings generally provide more accurate surface flux and horizontal advection terms compared to satellite and reanalysis-derived products.

a. Heat budget from Argo, satellite, and reanalysis products

We calculate h from Argo profiles using the criterion of a 0.1 kg m⁻³ increase in density (approximately equal to a 0.3°C decrease in temperature) referenced to the uppermost level of the profile, as long as it is shallower

than 10 m. The barrier layer thickness is defined as the difference between the isothermal layer depth, determined using a 0.3°C temperature criterion, and the mixed layer depth. We calculate T from Argo as the average temperature between the uppermost depth level and the base of the mixed layer.

The horizontal advection term requires knowledge of h , \mathbf{v} , and ∇T . Since direct measurements of \mathbf{v} are not available, we use satellite-based estimates from OSCAR. Foltz et al. (2012) found that the annual mean and seasonal variability of zonal currents from OSCAR agree reasonably well with direct measurements from PIRATA moorings. The meridional currents from OSCAR showed similar annual means compared to PIRATA, though the seasonal variability was less well represented. In section 4, it is shown that the contribution from horizontal advection is likely small compared to the other terms in (1) at most locations in the NETA, so uncertainties in OSCAR currents are not expected to dominate ϵ . Independent estimates of advection using the drifting buoy currents support this interpretation. Horizontal gradients of T are estimated from TMI SST using 2° centered differences.

The Q_0 term in (1) consists of LHF, SHF, SWR corrected for the penetrative component, and LWR. The LHF, SHF, and SWR terms are obtained from TropFlux, and the penetrative component of SWR is calculated following Morel and Antoine (1994), Sweeney et al. (2005), and Foltz and McPhaden (2009) using the 1998–2009 monthly mean seasonal cycle of chlorophyll- a concentration from SeaWiFS. Net LWR from the NCEP–NCAR reanalysis is corrected for mean biases using LWR from the 11.5°N , 23°W and 0° , 23°W PIRATA moorings. The moorings measure downwelling radiation, and the upwelling component is calculated as $0.97\sigma T_s^4$, where 0.97 is the emissivity of seawater, σ is the Stefan–Boltzmann constant, and T_s is SST from the mooring. The mean bias in net LWR at 0° , 23°W is 18 W m^{-2} (too much net emission from NCEP–NCAR reanalysis). The July–November mean bias at 11.5°N , 23°W is also 18 W m^{-2} . These months are chosen because there is frequent rainfall to rinse the radiometer dome. During boreal winter and spring, in contrast, there is significant accumulation of dust on the radiometers, which biases the SWR and LWR measurements (Foltz et al. 2013). We therefore correct the NCEP–NCAR reanalysis net LWR emission by subtracting a constant 18 W m^{-2} at each grid point in the NETA region.

The heat balance residual (ϵ) is calculated as the difference between the heat storage rate and the sum of horizontal advection and the net surface heat flux. Negative values of ϵ therefore indicate cooling from vertical turbulent mixing and entrainment, after accounting for

errors in the other terms in the heat balance (see the appendix for details of the error analysis).

b. Heat budget from PIRATA measurements

To calculate mixed layer depth, barrier layer thickness, and vertically averaged temperature in the mixed layer from the PIRATA mooring data, first missing values of temperature and salinity between 5 and 120 m are filled using vertical linear interpolation between adjacent depth levels. If temperature or salinity at 1 m is missing, it is first filled with temperature or salinity, respectively, from a depth of 5 m, and then the remaining gaps are filled with values from 10 m. The mixed layer depth, barrier layer thickness, and vertically averaged temperature are then calculated using the methodology described in the previous subsection, except a reference level of 1 m is used to define the mixed layer and isothermal layer depths.

Horizontal advection is calculated using daily mean mixed layer depth and horizontal velocity at a depth of 10 m from the PIRATA moorings, together with TMI SST gradients calculated using centered differences of 2° longitude and latitude. To calculate Q_0 we use downwelling SWR measurements from the moorings and assume an albedo of 6% (Payne 1972). At 20.5° and 11.5°N the SWR time series are corrected for dust accumulation biases using the MERRA clear-sky method described in Foltz et al. (2013). Because of large time-dependent biases at these locations (up to 100 W m^{-2}), we expect a high degree of uncertainty in the bias-corrected SWR. The penetrative component of SWR is calculated using the chlorophyll-dependent method described in the previous subsection.

The LHF and SHF are calculated with version 3 of the Coupled Ocean–Atmosphere Response Experiment (COARE) bulk algorithm (Fairall et al. 2003) using mooring air temperature, relative humidity, wind speed, and SST. Missing values of air temperature, relative humidity, and wind speed are replaced with the corresponding daily mean values from the NCEP–NCAR reanalysis. The daily mean seasonal cycles of the reanalysis data at each mooring location are first corrected for seasonally varying biases by comparing to the corresponding daily mean seasonal cycles from the moorings. We use direct measurements of downwelling LWR from the 0° , 23°W mooring and calculate the upwelling component as described in the previous subsection. At the 4° , 11.5° , and 20.5°N mooring locations, we use the bias-corrected NCEP–NCAR reanalysis LWR. The heat balance residual (ϵ) is calculated as in the previous subsection.

Daily averaged values of each term in (1) are computed using all available data at a given mooring location. The

daily values are then averaged to monthly means, and these values are averaged for each calendar month to form a monthly mean seasonal cycle. Error bars for each term in (1) are estimated as $e_{\text{tot}} = \sqrt{e_{\text{inst}}^2 + e_{\text{samp}}^2}$, where e_{inst} represents instrumental error, calculated using the methodology described in Foltz and McPhaden (2009), and e_{samp} is sampling error, calculated as the standard error of all monthly means for a given calendar month.

4. Results

In this section, we first discuss the seasonal cycle in the NETA based on satellite and reanalysis products and Argo. The mixed layer heat balance in the NETA is then analyzed, and the residual is interpreted in terms of physical processes and uncertainties associated with the other terms in (1).

a. Seasonal cycle of the northeastern tropical Atlantic

To illustrate the dominant features of the seasonal cycle in the NETA, mean conditions during April and September are shown in Fig. 1. April and September are the months when the ITCZ, defined as the latitude of maximum rainfall, on average is located at its southernmost and northernmost positions, respectively (Mitchell and Wallace 1992; Chiang et al. 2002). Throughout the year the warmest SST and lowest surface wind speeds generally coincide with the position of the ITCZ. In April the ITCZ is centered near 3°N in the central tropical Atlantic, with significant rainfall of at least 10 cm month⁻¹ extending southward to 5°S and northward to 5°N (Fig. 1a). There is a dramatic decrease in SST from ~29°C at 3°N to ~21°C at 25°N.

A sharp meridional gradient of rainfall is present at the northern edge of the ITCZ during April, associated with a pronounced increase in SWR from less than 200 W m⁻² at 3°N to 250 W m⁻² at 10°N (Figs. 1a,b). In contrast, there is a more gradual increase in SWR southward from 3°N, consistent with the more gradual decrease in rainfall. Elevated levels of African dust aerosol optical thickness ($\tau_{\text{dust}} > 0.2$) are present throughout most of the NETA. Maxima of 0.5–0.6 occur in a band extending southwestward from 10°N, 18°W to 8°N, 28°W (Fig. 1b), consistent with Kaufman et al. (2005).

Surface winds and associated wind stress curl and Ekman pumping during April maintain a shallow thermocline ($Z_{20} < 70$ m) in the southern half of the NETA (2°N–15°N) (Siedler et al. 1992; McClain and Firestone 1993; Fig. 1c). Thermocline depth in the NETA increases northward from 15°N and westward from the African coast, reaching a maximum of 150 m at 25°N, 28°W. The

deeper thermocline in the northwestern NETA is consistent with Ekman downwelling there (McClain and Firestone 1993). Surface currents in the NETA during April are dominated by westward Ekman flow to the north of 10°N and weaker and more variable flow to the south.

The thinnest mixed layer (<20 m) during April is found in the southern half of the NETA region, where winds are weakest (Fig. 1d). The mixed layer depth increases northward in the NETA and reaches 35 m at 25°N. The region with the thickest mixed layer between 20° and 25°N also experiences a thick barrier layer (>30 m), consistent with Tanguy et al. (2010). The barrier layer is maintained by the combination of northward advection of low-salinity water from the ITCZ and the subduction and southward movement of subtropical salinity-maximum water from the subtropical North Atlantic (e.g., Balaguru et al. 2012; Mignot et al. 2012). There is a thinner barrier layer in the southern NETA region (<20 m) that is most likely maintained by strong precipitation associated with the ITCZ.

The NETA undergoes pronounced changes between April and September. The core of the ITCZ moves from 3° to 7°N, and significant rainfall (>10 cm month⁻¹) extends to 15°N rather than 5°N (Figs. 1a,e). SST decreases markedly on the equator between April and September and increases significantly between 15° and 25°N. As a result, SST is more uniform within the NETA during September, ranging from 24° to 28°C, compared to a range of 20°–29°C in April. The more northward positions of the ITCZ and τ_{dust} in September compared to April contribute to a reduction in SWR between 5° and 25°N (Figs. 1b,f). A zonal band of Ekman upwelling associated with the ITCZ also moves northward between April and September, strengthening the Guinea thermocline dome and its associated cyclonic surface flow centered at 12°N, 25°W (Siedler et al. 1992; McClain and Firestone 1993; Yamagata and Iizuka 1995; Figs. 1c,g). In contrast, between the equator and 7°N Z_{20} increases from 50–70 to 70–100 m between April and September, and surface currents become eastward within the North Equatorial Countercurrent. The barrier layer thickens to 20–30 m between the equator and 7°N between April and September (Figs. 1d,h), driven by the combination of rainfall and the eastward transport of low-salinity water from the mouth of the Amazon River.

In summary, there are pronounced seasonal changes in the NETA that likely contribute to seasonal variability of the mixed layer heat budget. The changes are driven to a large extent by the meridional movement of the ITCZ, and the seasonal cycle therefore varies most strongly meridionally and is much more uniform zonally.

b. Mixed layer heat balance

Given the strong meridional dependence in the seasonality of the NETA, we first consider the mixed layer heat balance as a function of calendar month and latitude, averaged zonally between 18° and 28°W and with the annual mean removed (Fig. 3). The seasonal cycle of the mixed layer heat storage rate is strongest in the northern half of the NETA region (12°–25°N), where it exhibits a strong annual signal that peaks in boreal spring and summer (Fig. 3a). Results from the 11.5°N, 23°W and 20.5°N, 23°W moorings also show strong annual cycles in heat storage rate that reach maxima in July (Table 1). In contrast, the seasonal amplitude of the storage rate is much weaker between the equator and 10°N and a semiannual signal is more apparent, in agreement with the results from the 0°, 23°W and 4°N, 23°W moorings (Table 1).

The seasonal cycle of SWR varies in phase with the seasonal cycle of the heat storage rate throughout most of the NETA (Fig. 3b, Table 1). Variations of the amount of SWR absorbed in the mixed layer (Fig. 3b, contours) agree well with those of SWR (Fig. 3b, shading), indicating that the seasonal cycle of absorbed SWR is dominated by changes in SWR and not changes in mixed layer depth. The seasonal cycle of SWR itself results from a combination of changes in the solar zenith angle, water vapor, and other trace gases (e.g., carbon dioxide and ozone), clouds, and aerosols (Fig. 4). The combination of the zenith angle and trace gases dominates the seasonal cycle of SWR between 15° and 25°N with a peak-to-peak amplitude of 100–150 W m⁻² (Fig. 4a).

Between the equator and 15°N forcing from clouds is comparable in magnitude to forcing from the combination of zenith angle and trace gases. The seasonal cycle of cloudiness is most important immediately to the north of the mean position of the ITCZ (7°–15°N), where the peak-to-peak amplitude of cloud forcing is 60–100 W m⁻². This region experiences the lowest cloud cover during boreal winter and spring, when the ITCZ is farthest south, and higher cloud cover during boreal summer and fall when the ITCZ is close to its northernmost latitude (Fig. 4b). In contrast, between the equator and 7°N the seasonal cycle of cloud forcing is weaker (peak-to-peak amplitude of 20–60 W m⁻²) because of persistent high-level cloud cover between 2° and 7°N and a peak in low-level cloudiness on the equator during boreal summer, when high cloud cover is at a minimum there (Klein and Hartmann 1993). The seasonal cycle of aerosol forcing is significantly weaker than forcing from either the sum of the zenith angle and trace gases or clouds, with a maximum peak-to-peak amplitude of 15–20 W m⁻² between 10° and 20°N (Fig. 4c).

The seasonal cycle of LHF generally varies in phase with that of SWR between 5° and 25°N: evaporative cooling is weakest during boreal summer and strongest during boreal winter (Fig. 3c; Table 1). In contrast, between the equator and 5°N, LHF tends to vary out of phase with SWR. The out-of-phase relationship in this region can be explained by the relationships among the ITCZ, cloudiness, and wind speed: when the ITCZ is at its northernmost latitude in boreal summer and fall (~7°N), cloudiness is low and SWR is high between 0° and 5°N, whereas wind speed is high and evaporative cooling is therefore strong in the same latitude band. The seasonal cycle of the air–sea humidity gradient also affects the seasonality of LHF, especially between 20° and 25°N where LHF is not well correlated with wind speed (Fig. 3c). The low correlation between LHF and wind speed in this region implies that there is weak wind–evaporation–SST feedback on seasonal time scales.

The phasing of the seasonal cycle of the net surface heat flux (Fig. 3d), which is the sum of absorbed SWR and LHF as well as much smaller contributions from LWR and SHF, agrees well with the phasing of the mixed layer heat storage rate (Fig. 3a), suggesting that at most latitudes changes in mixed layer temperature are driven primarily by the net surface heat flux. The contribution from horizontal heat advection is much weaker than that of the net surface heat flux at all latitudes in the NETA when averaged zonally, supporting this interpretation (Fig. 3e). We note, however, that horizontal advection may be underestimated between the equator and ~5°N during boreal summer because the 5-day OSCAR currents likely do not fully resolve the strong velocity and SST signals associated with tropical instability waves, which tend to warm the mixed layer (Grodky et al. 2005). The causes of the larger seasonal variability of horizontal advection from the current meter measurements at the 20.5°N, 23°W mooring location (Table 1) compared to the zonally averaged values from OSCAR will be addressed in section 4c.

Between 15° and 25°N the peak-to-peak amplitude of the seasonal cycle of the sum of the net surface heat flux and horizontal heat advection is larger than the amplitude of the heat storage rate, resulting in a seasonal peak-to-peak amplitude of the residual of 70–90 W m⁻² (Fig. 3f, Table 1). The amplitude of the seasonal cycle of the residual between 15° and 25°N is even larger when the drifter analysis is used to calculate advection instead of OSCAR. The larger amplitude of the residual occurs because the seasonal cycle of horizontal advection calculated using the drifter analysis is similar in terms of phase and has a slightly larger amplitude compared to the OSCAR analysis (the drifter analysis gives amplitudes typically 5–15 W m⁻² larger, peak-to-peak, with a

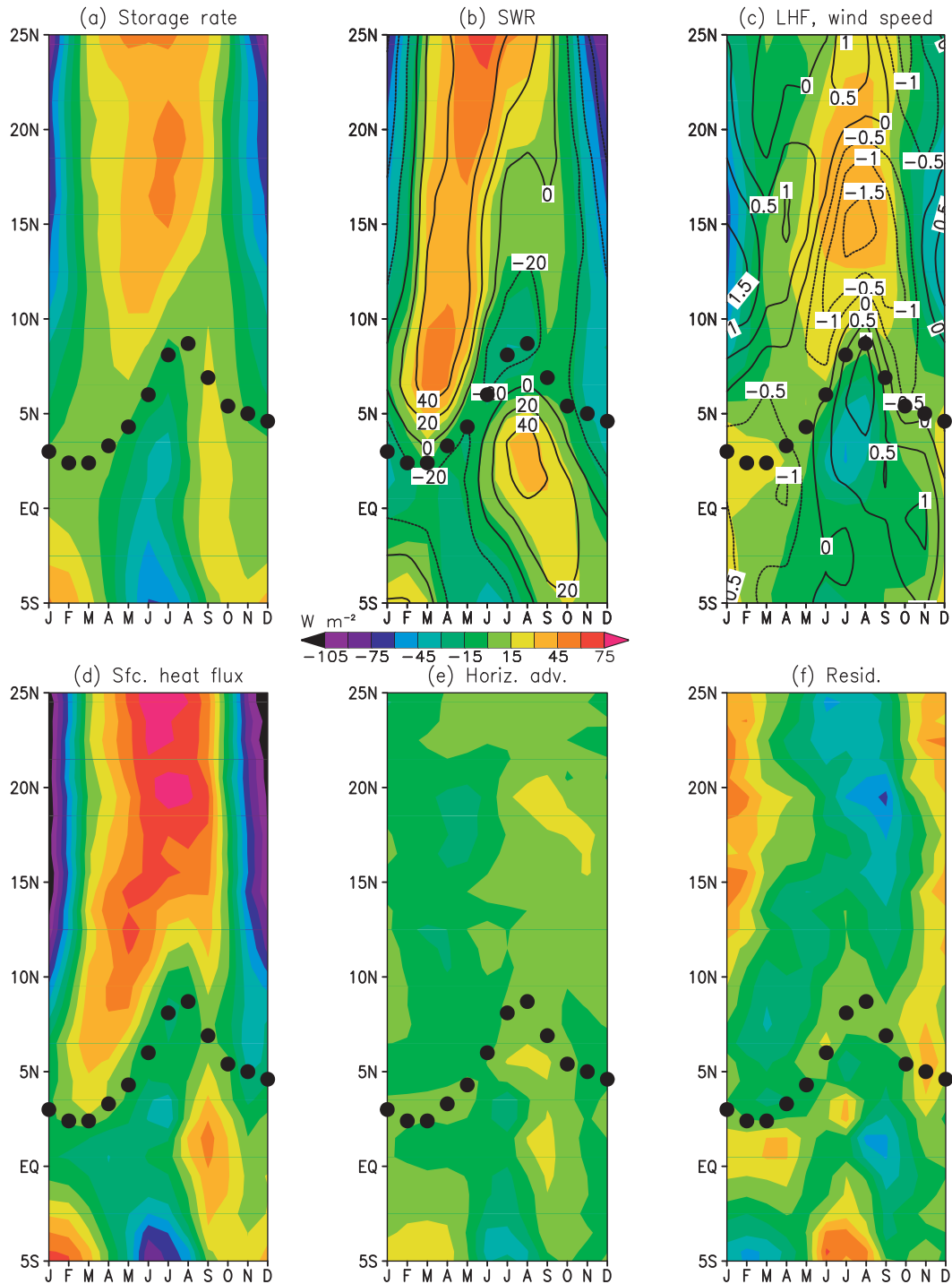


FIG. 3. Latitude–time plots of the terms in the mixed layer heat balance after removing the annual mean at each grid point and averaging between 18° and 28°W: (a) mixed layer heat storage rate. (b) Surface shortwave radiation (SWR, shaded) and SWR absorbed in the mixed layer (contours), (c) surface latent heat flux (LHF, shaded) and wind speed ($m s^{-1}$, contours), (d) net surface heat flux (Q_0), (e) horizontal mixed layer heat advection based on velocity from the OSCAR product, and (f) heat balance residual (all flux units: $W m^{-2}$). Black dots in (a)–(f) represent the position of the ITCZ based on the latitude of maximum rainfall and averaged between 18° and 28°W.

TABLE 1. Mean, annual, and semiannual harmonics of the terms in the heat balance at four PIRATA mooring locations in the northeastern tropical Atlantic. For each location, rows 1–8 show the mixed layer heat storage rate (Stor), zonal advection (Uadv), meridional advection (Vadv), surface shortwave radiation (SWR), shortwave radiation absorbed in the mixed layer (Abs SWR), latent heat flux (LHF), sum of sensible heat flux and net longwave radiation (LWR+SHF), and residual (Res) (heat storage rate minus the sum of the net surface heat flux and horizontal advection). Columns 3–7 show the record-length mean peak-to-peak amplitude of the annual cosine harmonic (A_{ann}), calendar month of the maximum of the annual cosine harmonic (M_{ann}), peak-to-peak amplitude of the semiannual cosine harmonic (A_{semi}), calendar month of the first maximum of the semiannual cosine harmonic (M_{semi}), and variance explained (Var) by the sum of the annual and semiannual harmonics. (Units: W m^{-2} for columns 1–5 and % for column 6.) Positive values indicate a warming tendency for the mixed layer.

Term	Mean	A_{ann}	M_{ann}	A_{semi}	M_{semi}	Var
20.5°N, 23°W						
Stor	−20	135	7	55	4	95
Uadv	−30	55	7	55	4	64
Vadv	5	5	11	10	6	34
SWR	220	100	6	45	4	98
Abs SWR	210	90	6	35	5	98
LHF	−115	50	8	20	3	93
LWR+SHF	−45	25	7	10	3	97
Res	−45	75	1	45	1	62
11.5°N, 23°W						
Stor	−10	65	7	30	5	86
Uadv	5	5	5	15	6	33
Vadv	5	25	1	15	1	58
SWR	225	60	5	40	4	95
Abs SWR	200	60	5	35	4	97
LHF	−95	75	7	20	4	97
LWR+SHF	−50	25	8	0	3	98
Res	−75	45	12	20	6	72
4°N, 23°W						
Stor	5	30	10	65	4	58
Uadv	−5	20	9	10	1	60
Vadv	−10	20	3	35	4	24
SWR	205	35	8	40	3	79
Abs SWR	185	45	8	60	3	78
LHF	−105	55	2	25	5	86
LWR+SHF	−45	5	3	5	6	86
Res	−15	45	10	5	1	47
0°, 23°W						
Stor	0	50	11	35	3	83
Uadv	−5	15	12	25	4	83
Vadv	−5	15	3	20	6	41
SWR	250	40	9	15	4	95
Abs SWR	230	70	10	10	5	98
LHF	−75	15	4	10	3	90
LWR+SHF	−40	10	2	5	5	94
Res	−105	20	1	30	3	32

maximum increase in amplitude of 30 W m^{-2} at 20°N). The large seasonal cycle of the residual implies an important role for the combination of vertical turbulent mixing and errors in the net surface heat flux, storage, and advection terms.

c. Heat balance residual in the trade wind and ITCZ core regions

To examine the causes of the seasonal cycle of the residual and its strong dependence on latitude, in this section we focus on two regions in the NETA with distinctly different seasonal cycles of the residual (Fig. 5): the trade wind region ($15^\circ\text{--}25^\circ\text{N}$) and the ITCZ core region ($3^\circ\text{--}8^\circ\text{N}$). In addition to encompassing areas with different seasonal cycles of the residual, the trade wind and ITCZ core regions include the locations of the 20.5° and 4°N PIRATA moorings, enabling meaningful comparisons to the heat budgets at these locations. The averaging for the trade wind and ITCZ core regions is performed over a broad range of latitudes in order to minimize random sampling errors and thus produce robust results. In section 4d, we consider the residual along the equator.

The trade wind region is characterized by strong seasonal cycles of the residual and barrier layer thickness that vary approximately in phase, with minima in boreal summer and fall and maxima in boreal winter (Fig. 5). The in-phase relationship between the residual and barrier layer thickness in the trade wind region (i.e., the barrier layer tends to be thickest when cooling from the residual is weakest and vice versa) suggests that the barrier layer may exert a significant influence on vertical turbulent mixing at the base of the mixed layer and, hence, the residual through its impact on the vertical temperature gradient beneath the mixed layer (e.g., Pailler et al. 1999; Foltz and McPhaden 2009). However, there is also a large seasonal cycle of barrier layer thickness in the ITCZ core region that coincides with a much weaker seasonal cycle of the residual, indicating that other factors must be controlling the residual here or that the seasonal cycle of the residual in both regions may be driven instead by the accumulation of errors from the other terms in (1).

To investigate the possibility that the seasonal cycle of the residual results primarily from the sum of errors in the net surface heat flux, heat storage, and horizontal advection terms in (1), we compare the heat budgets averaged in the trade wind and ITCZ core regions to the heat budgets from the 20.5°N , 23°W and 4°N , 23°W PIRATA moorings. The heat budget terms at 20.5°N , 23°W agree well with those in the trade wind region during February–October (Fig. 6). During these months the sum of the net surface heat flux and horizontal heat

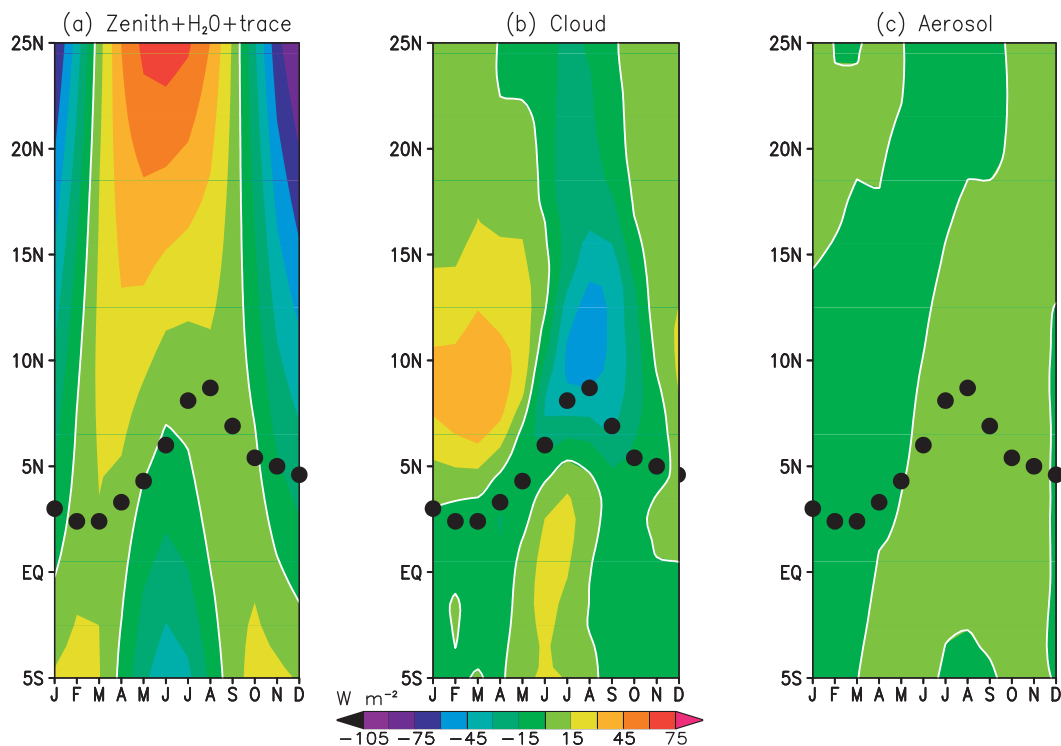


FIG. 4. As in Fig. 3, but for SWR (W m^{-2}) forced by (a) the combination of the solar zenith angle, water vapor, and trace gases (calculated from the MERRA clean clear-sky product), (b) clouds (total SWR from MERRA minus the clear-sky SWR), and (c) aerosols (total SWR from MERRA minus the clean sky SWR).

advection is significantly larger than the heat storage rate, resulting in negative values of the residual. During November–January, horizontal advection at the mooring location varies from -25 to -125 W m^{-2} compared to -15 to 0 W m^{-2} in the trade wind region. The difference is due primarily to stronger currents measured by the mooring compared to those estimated by OSCAR and by the drifting buoy analysis. The differences are also present when the same time period is used for the calculation instead of the monthly climatologies based on all available data. It is therefore possible that OSCAR and the drifting buoy analysis underestimate near-surface currents, and hence cooling from horizontal advection, in the trade wind region during boreal winter. It is also possible that mesoscale variability at the mooring is aliased into the seasonal cycle, resulting in stronger currents and larger negative values of horizontal advection during boreal winter at the mooring location compared to the average in the trade wind region. Longer velocity records from the mooring are needed to resolve this discrepancy. However, it will always be difficult to compare advection from the mooring to the estimates from OSCAR and the drifting buoy analysis because the datasets do not resolve the same spatial and temporal scales. Despite the differences in horizontal advection, the residual has a similar

seasonal cycle and amplitude in the trade wind region compared to those at the mooring location. We therefore have confidence that the seasonal cycle of the residual is driven primarily by physical processes and not accumulated errors from the other terms in (1).

The heat budget at the 4°N , 23°W PIRATA mooring location is similar to the heat budget in the ITCZ core region, though there are noticeable differences in the SWR, LHF, and horizontal advection terms (Fig. 7). During boreal summer and fall SWR is higher at 4°N , 23°W compared to SWR averaged in the ITCZ core region. The difference is caused by the positioning of the ITCZ and associated cloudiness to the north of 4°N during those seasons, which results in lower SWR averaged between 3° and 8°N compared to at 4°N . The seasonality of the ITCZ location also explains why evaporative cooling during boreal summer and fall is stronger (i.e., LHF is more negative) at 4°N , 23°W compared to LHF in the ITCZ core region: the more northerly position of the ITCZ during boreal summer and fall leads to stronger wind-induced evaporative cooling at 4°N compared to the 3° – 8°N average. Finally, seasonal variability of horizontal heat advection is considerably stronger at 4°N , 23°W compared to the ITCZ core region, though the phasing is similar. Stronger variability at the

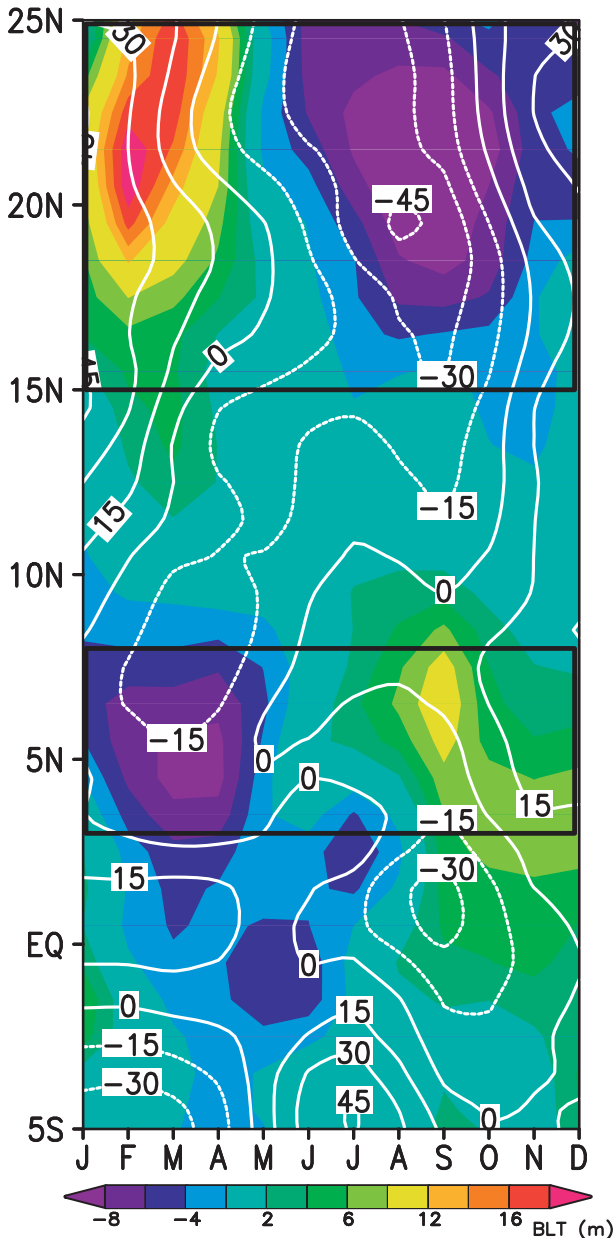


FIG. 5. As in Fig. 3, but shading is for the barrier layer thickness and contours are the heat balance residual (W m^{-2}). The annual mean of each quantity at each grid point has been removed. Black boxes enclose the trade wind (15° – 25°N) and ITCZ core (3° – 8°N) regions.

mooring location is expected since there is no spatial averaging to smooth the time series. Despite differences in SWR, LHF, and advection, both time series show a period during February–April when the sum of the net surface heat flux and advection exceeds the heat storage rate by 15 – 50 W m^{-2} , resulting in negative values of the residual. It is therefore likely that the residual during February–April results primarily from physical processes

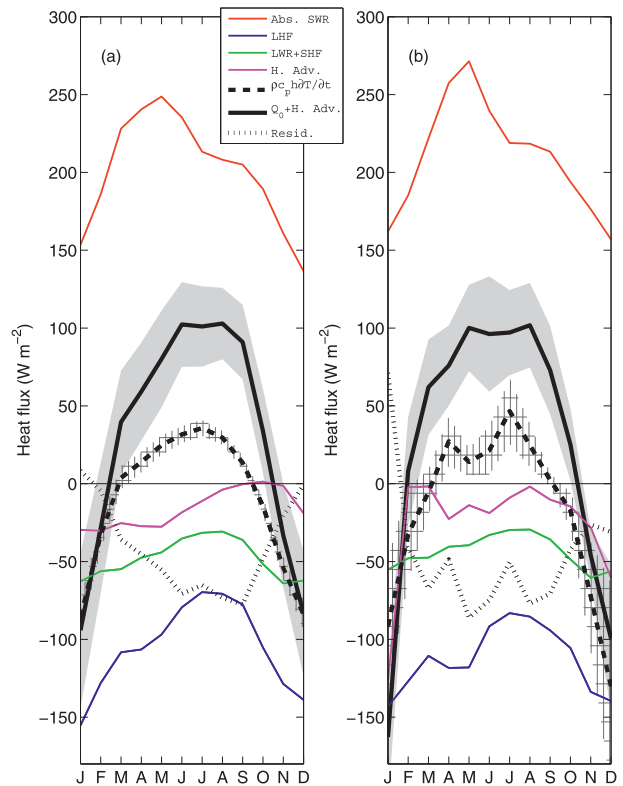


FIG. 6. Terms in the mixed layer heat balance (a) averaged in the region 15° – 25°N , 18° – 28°W and (b) at the 20.5°N , 23°W PIRATA mooring location. Shown are the shortwave radiation absorbed in the mixed layer (Abs. SWR, red curve), latent heat flux (LHF, blue curve), sum of longwave radiation and sensible heat flux (LWR+SHF, green curve), horizontal heat advection (purple curve), storage rate (dashed black curve), sum of the net surface heat flux and horizontal advection (solid black), and the residual (storage rate minus the sum of the net surface heat flux and horizontal advection, dotted black curve). Gray shading and hatching indicate one standard error for the sum and storage terms, respectively.

and not errors in the other terms in (1). During boreal summer there is more uncertainty in the residual because of uncertainties in eddy heat advection.

The most likely candidate for the seasonal cycles of the residual in the trade wind and ITCZ core regions is the heat flux across the base of the mixed layer due to vertical turbulent mixing (including the process of entrainment), which depends on the rate of turbulent mixing at the base of the mixed layer and the temperature difference between the mixed layer and the water beneath:

$$Q_{-h} \propto \Delta T w_e. \quad (2)$$

Here, ΔT is the temperature jump between the mixed layer and the temperature beneath, and w_e is the rate of vertical turbulent mixing at the base of the mixed layer.

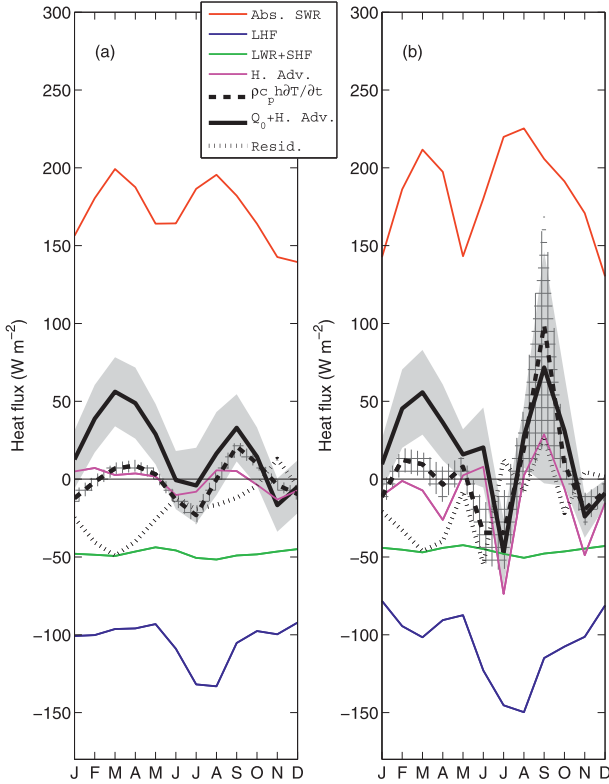


FIG. 7. As in Fig. 6, but (a) averaged in the region 3°–8°N, 18°–28°W and (b) at the 4°N, 23°W PIRATA mooring location.

The w_e term in (2) depends on a number of factors, such as the strength of surface wind- and buoyancy-induced turbulent mixing, the current shear and stratification below the mixed layer, and the temperature jump at the base of the mixed layer (e.g., Kraus and Turner 1967; Niiler and Kraus 1977):

$$w_e(\text{NK}) = \frac{2mu_*^3 + \frac{h}{2}[(1+n)B_0 - (1-n)|B_0|] + (h-2/\gamma)J_0}{c_i^2 - s(\Delta\mathbf{v})^2}. \quad (3)$$

In (3), $u_* = \sqrt{\tau/\rho}$ is friction velocity (τ is the surface wind stress magnitude and ρ is the density of seawater), h is mixed layer depth, B_0 is surface buoyancy flux, $1/\gamma$ is the shortwave extinction depth, $J_0 \equiv [g\alpha/(\rho c_p)]I_0$ (I_0 is the surface shortwave radiation), $c_i^2 = \Delta b h$ [$\Delta b = g(\rho_{-h} - \rho_a)/\rho_0$ is the buoyancy averaged in the mixed layer relative to the buoyancy at the base of the mixed layer], and $\Delta\mathbf{v}$ is vertically averaged horizontal mixed layer velocity relative to velocity at the base of the mixed layer. The terms represent, from left to right, turbulence generation due to wind, surface buoyancy flux, and the penetrative

component of solar radiation. Each term is scaled by stratification and vertical velocity shear: stronger stratification and weaker shear tend to reduce the magnitude of w_e , whereas weaker stratification and stronger shear tend to increase the magnitude of w_e . The constants m , n , and s are empirically determined proportionality factors.

Here we consider a simplified form of (3) in which turbulent mixing depends only on u_*^3 and h (i.e., $B_0 = 0$, $J_0 = 0$, $\Delta\mathbf{v} = 0$, and $\Delta b = 1$):

$$w_e \propto \frac{u_*^3}{h}. \quad (4)$$

The justification for setting $\Delta\mathbf{v} = 0$ is based on the observation that vertical current shear is large only very close to the equator (e.g., Brandt et al. 2006). The rationale for neglecting seasonal variations of Δb is that we use a constant density criterion to define the mixed layer so that Δb is not expected to change significantly. Neglecting B_0 cannot be justified based on scaling arguments, but is done to simplify the analysis since there is significant uncertainty in the value of n in (3). Instead, the likely importance of B_0 is discussed later in this section in relation to the wind forcing represented in (4). Since there is large uncertainty associated with the definition of ΔT in (2), for simplicity we assume that ΔT depends on the barrier layer thickness, which reflects the magnitude of the temperature jump at the base of the mixed layer (e.g., Foltz and McPhaden 2009), and Z_{20} , which is an indicator of the temperature at a depth of ~ 20 – 70 m below the base of the mixed layer.

The seasonal cycles of barrier layer thickness, Z_{20} , and vertical turbulent mixing explain seasonal variations of the residual reasonably well in the trade wind region (Figs. 8a–c). The largest negative values of the residual occur during June–September (about -70 W m^{-2} on average), when the barrier layer thickness is close to its seasonal minimum (< 15 m) and the rate of vertical turbulent mixing is close to its seasonal maximum ($> 3 \times 10^{-8} \text{ m s}^{-1}$). The maximum in the rate of turbulent mixing results primarily from a corresponding minimum in the mixed layer depth. In contrast, Z_{20} tends to vary in quadrature with the residual and therefore does not seem to exert a strong influence on the residual, possibly because Z_{20} is large (> 85 m) throughout the year. The turbulence due to the surface buoyancy flux is driven mainly by SWR and LHF and has a strong annual cycle (implied by Fig. 6) that varies approximately 180° out of phase with the residual. Changes in the surface buoyancy flux therefore cannot explain the seasonal phasing of the residual but may act to reduce its seasonal amplitude.

In the ITCZ core region, the annual mean of the residual is less negative than in the trade wind region. This

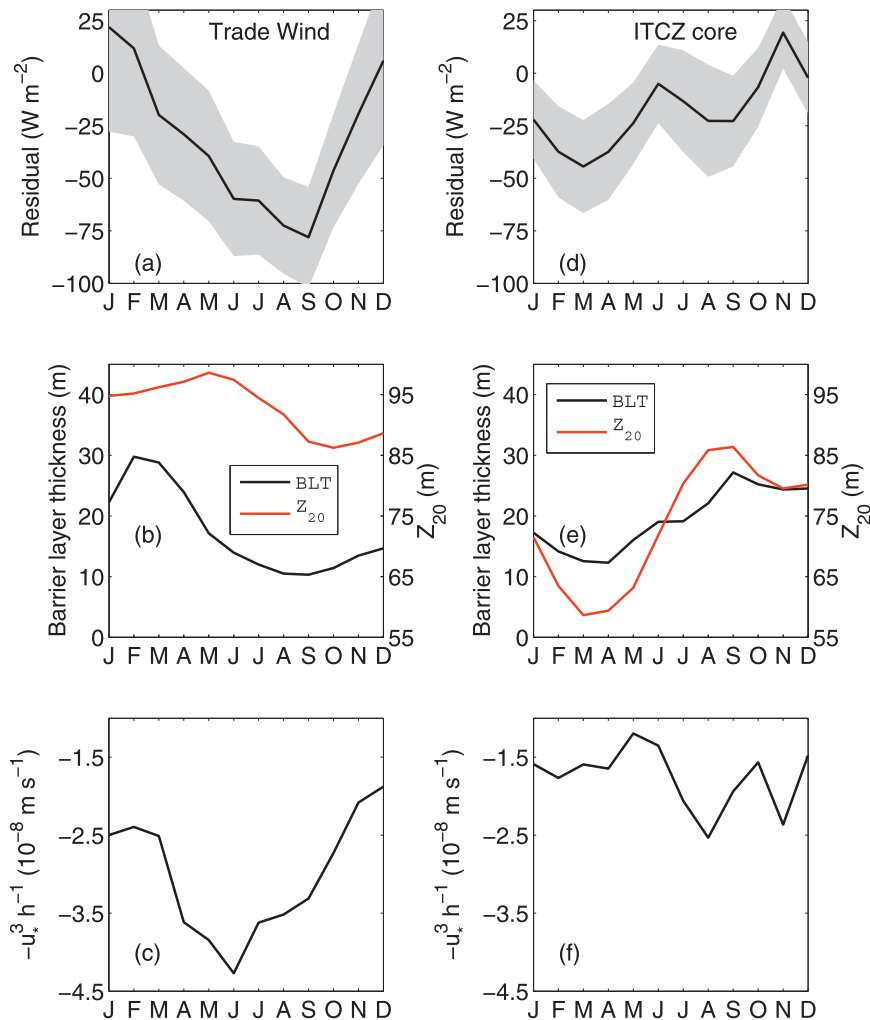


FIG. 8. Monthly seasonal cycles, averaged in the trade wind region shown in Fig. 5, of the (a) heat balance residual, (b) barrier layer thickness (black) and depth of the 20°C isotherm (red), and (c) rate of turbulent mixing due to the wind (w_e). The sign of w_e has been reversed so that w_e varies in the same sense as the residual in (a); that is, larger negative values of w_e are associated with larger negative values of the residual. (d)–(f) As in (a)–(c), but averaged in the ITCZ core region shown in Fig. 5.

is consistent with a smaller annual mean value of the rate of vertical turbulent mixing in the ITCZ core region (Fig. 8f). In the ITCZ core region the largest negative residual (about -30 W m^{-2}) occurs during February–April and is likely driven by corresponding minima in barrier layer thickness and Z_{20} (Fig. 8b). The turbulence generation due to the surface buoyancy flux in the ITCZ core region is largest during boreal spring, when evaporative cooling is weak and heating from SWR is strong (Fig. 7), and is therefore approximately 180° out of phase with barrier layer thickness and Z_{20} . This out-of-phase relationship, combined with the weak seasonal cycle of vertical turbulent mixing, possibly explains why the seasonal cycle of the residual in the ITCZ core region

is so much weaker than in the trade wind region despite similar seasonal amplitudes of barrier layer thickness and Z_{20} .

As a consistency check on the residual in the trade wind and ITCZ core regions, it is useful to consider the associated vertical diffusivity coefficients:

$$K_v = \frac{\epsilon}{\rho c_p \partial T / \partial z}. \quad (5)$$

Here, ϵ is the heat balance residual and $\partial T / \partial z$ is the average vertical temperature gradient between the base of the mixed layer and 10 m below the base of the mixed layer. In the trade wind region, we find that the seasonal

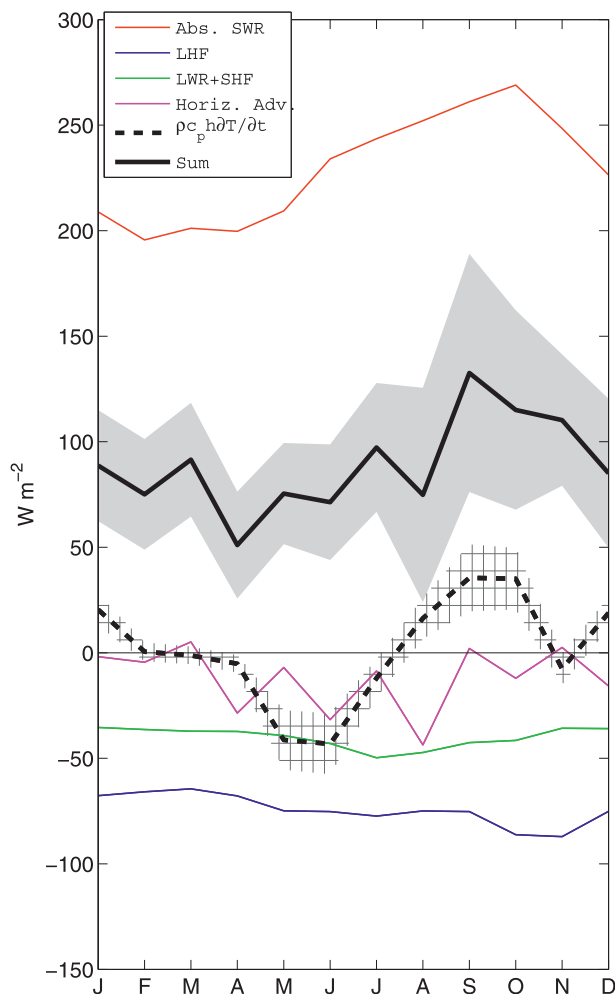


FIG. 9. As in Fig. 7b, but at the 0° , 23°W PIRATA mooring location.

cycle of K_v varies between 0.3 and $4.1\text{ cm}^2\text{ s}^{-1}$, with a maximum in March–June and minimum in November–January and an annual mean of $2.2\text{ cm}^2\text{ s}^{-1}$. In the ITCZ core region, K_v ranges from zero to $3.3\text{ cm}^2\text{ s}^{-1}$, with a mean of $1.2\text{ cm}^2\text{ s}^{-1}$ and no noticeable seasonal cycle. These values generally agree with those calculated by Foltz et al. (2010) in the ITCZ region of the southwestern Indian Ocean (0.9 – $2.5\text{ cm}^2\text{ s}^{-1}$) and by Wang and McPhaden (1999) in the equatorial Pacific (1.8 – $6.5\text{ cm}^2\text{ s}^{-1}$).

d. Heat balance residual on the equator

Similar to the zonally averaged heat budget along the equator (Fig. 3), at the 0° , 23°W mooring there are noticeable annual cycles of SWR and mixed layer heat storage rate and weaker seasonal variations of the remaining terms in the heat budget (Fig. 9, Table 1). For interpreting the residual in terms of physical processes, we therefore focus on the heat budget at the 0° , 23°W

mooring location since vertical profiles of horizontal currents are also available.

The residual reaches its largest negative values (from -130 to -120 W m^{-2}) in May–July and November and smallest negative values (-70 W m^{-2}) in April and August, though there are large error bars (20 – 50 W m^{-2}) throughout the year (Fig. 10a). The seasonal cycle of vertical shear of the current between the mixed layer and 20 m below the base of the mixed layer shares some similarities with that of the residual (small negative values in February and June–September and large negative values in May–June and October–November). It is therefore possible that changes in the vertical shear of the current drive part of the seasonal variability of the residual, with periods of largest vertical shear of the current generating the strongest turbulent mixing and hence contributing to the increased negative heat flux through the base of the mixed layer.

The large negative residual in May–July also coincides with a maximum in the rate of turbulent mixing and a minimum in Z_{20} , which would tend to increase the temperature gradient beneath the mixed layer and, hence, the rate of cooling from turbulent mixing (Figs. 10b,c). In general, however, seasonal variations of the residual most closely match those of the vertical shear of the current and the vertical turbulent mixing rate, suggesting that the seasonal intensification of equatorial easterly wind stress in boreal spring drives stronger cooling from vertical mixing directly by increasing the rate of wind-induced mixing and indirectly by generating stronger westward surface currents and hence larger vertical current shear. These results are consistent with recent observational and modeling studies (Jouanno et al. 2011; Giordani et al. 2013; Hummels et al. 2013).

The seasonal cycle of the residual at 0° , 23°W translates to vertical diffusivity values of 2.5 – $5.2\text{ cm}^2\text{ s}^{-1}$ (the annual mean is $3.7\text{ cm}^2\text{ s}^{-1}$), which are larger than those found in the trade wind and ITCZ core regions. This is not surprising since vertical shear on the equator is expected to produce stronger turbulent mixing compared to that produced at the off-equatorial locations (Hummels et al. 2013). The values of vertical diffusivity that we find on the equator are consistent with those calculated by Wang and McPhaden (1999) in the eastern equatorial Pacific but are more than an order of magnitude larger than the values calculated by Gregg et al. (2003) near the equator in the central and western equatorial Pacific. The smaller values found by Gregg et al. (2003) may be due to the different location of the measurements and that their calculation only included mixing from the breaking of internal waves, whereas our residual includes all forms of vertical entrainment and mixing.

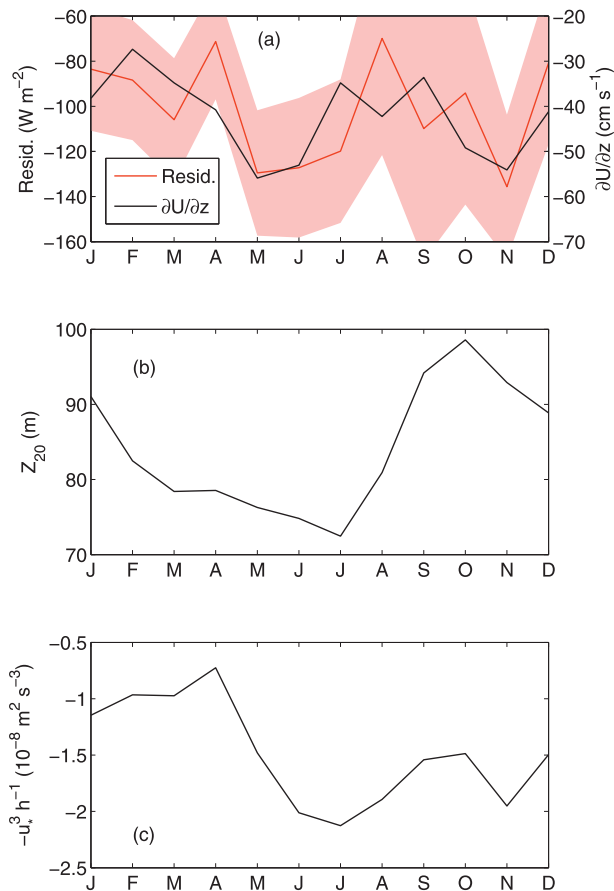


FIG. 10. Monthly seasonal cycles, at the 0° , 23°W PIRATA mooring location, of the (a) heat balance residual (red) and difference between horizontal current speed averaged in the mixed layer and 20 m below the mixed layer (black), (b) depth of the 20°C isotherm, and (c) rate of vertical turbulent mixing due to the wind (w_e).

5. Summary and discussion

The seasonal cycle of the mixed layer heat balance in the northeastern tropical Atlantic was assessed using in situ and satellite measurements together with output from atmospheric reanalyses. A strong latitudinal dependence of the heat budget was found, consistent with pronounced meridional variations of SST, winds, and solar radiation in the northeastern tropical Atlantic. Three distinct regimes within the northeastern tropical Atlantic were identified:

1) Trade wind (15° – 25°N): this region is characterized by a strong annual cycle of SST (range of 5°C). Changes in mixed layer heat storage result from a 180° out-of-phase relationship between warming from surface shortwave radiation driven by changes in the solar zenith angle, which is strongest in boreal summer, and surface evaporative cooling, which is weakest in

boreal summer. The surface heat flux–induced changes in mixed layer heat storage are damped by a strong annual cycle of cooling from vertical turbulent mixing, which reaches a maximum in boreal summer and a minimum in winter. The annual cycle of turbulent mixing is driven by an approximately out-of-phase relationship between the barrier layer thickness, which is thinnest and most conducive to turbulent mixing–induced cooling in late boreal summer, and wind-driven mixing, which is strongest in early summer.

2) ITCZ core (3° – 8°N): there is a weak seasonal cycle of SST in this region (range of 1.5°C) that is dominated by the semiannual harmonic. The weak semiannual cycle of mixed layer heat storage results from a semiannual cycle of surface shortwave radiation, with maxima in March and August, that is damped by surface evaporative cooling and vertical turbulent mixing. Surface evaporative cooling damps the summertime maximum in shortwave-induced warming, and a weaker maximum in turbulent mixing–induced cooling damps the springtime maximum. The peak in turbulent-mixing–induced cooling in boreal spring occurs when the thermocline is shallowest and the barrier layer is thinnest.

3) Equator: this location is situated to the south of the ITCZ throughout the year and experiences a moderate annual cycle of SST (range of 3.5°C). Changes in mixed layer heat storage are driven by an annual cycle of surface shortwave radiation that reaches a maximum in October and a minimum in February–April and a semiannual cycle of vertical turbulent mixing, which cools the mixed layer most strongly during May–July and November. Cooling from vertical mixing is driven by vertical current shear and local wind-forced turbulence. There is a weaker seasonal cycle of horizontal heat advection, which cools the mixed layer most strongly during April–August.

The mechanisms that dominate the heat budget in the northeastern tropical Atlantic are illustrated schematically in Fig. 11. Our results generally agree with those of Carton and Zhou (1997) and Yu et al. (2006), which show that the seasonal cycle of SST to the north of 10°N is driven primarily by the surface heat flux, while the seasonal cycle of SST near the equator results mainly from wind-driven upwelling. Despite the broad similarities, there are important differences in specific regions. In the ITCZ core region Yu et al. found that seasonal variations of Ekman divergence and associated upwelling contribute significantly to the seasonal cycle of SST. In contrast, we found that the weak seasonal cycle of SST results from a semiannual cycle of surface shortwave

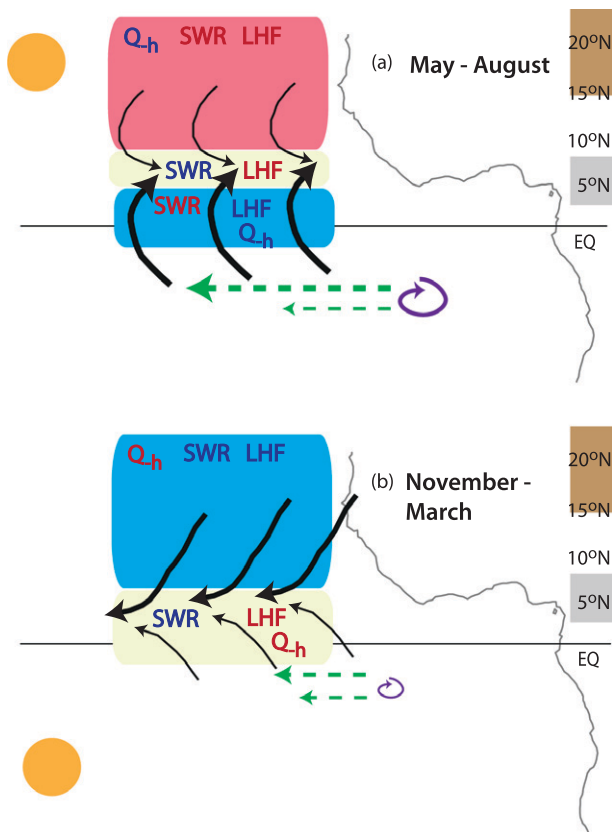


FIG. 11. Schematic diagram illustrating the processes driving the seasonal cycle of SST in the northeastern tropical Atlantic during (a) May–August and (b) November–March. The periods for (a) and (b) correspond to the most pronounced northward and southward movement of the ITCZ, respectively. Shading indicates the sign of the rate of change of SST: strong warming (red), strong cooling (blue), and weaker warming or cooling (yellow). The SWR, LHF, and Q_{-h} terms represent the contributions of shortwave radiation, latent heat flux, and vertical turbulent mixing, respectively, to the seasonal cycle of SST, with blue for cooling and red for warming, relative to the annual mean. Black arrows indicate surface wind direction, with longer and thicker arrows corresponding to higher speed. The length and thickness of the long dashed green arrows represent equatorial near-surface zonal current speed, and difference between long and short arrows indicates strength of vertical shear. Size of purple arrows shows strength of shear-induced vertical mixing. Orange circles represent the position of the sun. Brown and gray rectangles on the right show the latitudinal ranges of the trade wind and ITCZ core regions, respectively.

radiation that is damped by cooling from vertical mixing in boreal spring and by evaporative cooling in the summer. Our results in the ITCZ core agree well with the modeling results of Peter et al. (2006), which show an important role for the surface heat flux in this region and a smaller contribution from vertical processes that peak in February–April.

On the equator we found important contributions from shortwave radiation and vertical mixing, consistent

with Foltz et al. (2003), Peter et al. (2006), and Jouanno et al. (2011). The modeling studies of Peter et al. (2006) and Jouanno et al. (2011) show that horizontal advection plays only a minor role, while Foltz et al. (2003) and Giordani et al. (2013) found that it plays an important role in the formation of the cold tongue during boreal summer. Using direct measurements of velocity from the 0°, 23°W PIRATA mooring and estimates from OSCAR, we found much weaker advection compared to Foltz et al. We therefore conclude that cooling from zonal advection was overestimated in their study, possibly because their analysis relied heavily on measurements from surface-drifting buoys near the equator, where the number of drifter days is low and where strong velocities of tropical instability waves may have been aliased onto the seasonal cycle. The updated drifter climatology used in this study is also more consistent with direct measurements of currents from the 0°, 23°W PIRATA mooring, supporting the conclusion that the results of Foltz et al. (2003) were affected by a low density of drifter observations.

Though there are large error bars on our heat budget residual on the equator, its seasonal cycle generally agrees with the seasonal cycle of mixing found in the modeling studies of Peter et al. (2006) and Jouanno et al. (2011). The mechanisms also appear to be similar: strengthening of the surface winds in boreal spring and summer accelerates westward equatorial surface currents, leading to stronger shear between the mixed layer and the equatorial undercurrent. The stronger shear in turn generates more intense vertical turbulent mixing that acts to cool the mixed layer.

Our results generally agree with previous theories of the seasonal cycle in the equatorial and ITCZ core regions. We showed that the formation of the cold tongue at 23°W during boreal spring and summer is driven by enhanced cooling from turbulent mixing and, to a lesser extent, advection of cooler water from the east. These results are consistent with Mitchell and Wallace (1992) and Chang and Philander (1994). We found that SST under the ITCZ remains warm in the annual mean because of weak winds and associated weak turbulent mixing and evaporative cooling. Xie and Philander (1994) also suggest that SST remains warm under the ITCZ because of positive wind–evaporation–SST feedback and weak vertical mixing. Our results additionally show that the weak seasonal cycle under the ITCZ is due to damping of the shortwave-radiation-induced semiannual cycle of SST by evaporative cooling in the boreal summer and vertical mixing in boreal spring.

Despite the general consistency between our results based on Argo, satellite, and reanalysis data and the results using measurements from PIRATA, considerable

uncertainty remains regarding the magnitude of zonal heat advection between 10°–20°N and meridional advection in the ITCZ core region. There are also large error bars on the residual terms in the ITCZ core region and at the 0°, 23°W mooring location. Because of the large error bars, numerical modeling experiments and heat budget analyses using ocean reanalysis products (e.g., Zhu et al. 2012) will be useful for verifying the seasonal cycles of horizontal advection and vertical turbulent mixing in these regions. It is expected that the uncertainties in the observational analyses will be reduced as the Argo and drifter datasets expand and as velocity, temperature, and surface flux records from PIRATA increase in length.

The results of this study may have implications for understanding interannual and longer time scale variability in the tropical Atlantic. The maximum in cooling from turbulent mixing in the ITCZ region occurs in boreal spring when the Atlantic meridional mode (AMM) is most active. Since the mechanisms of the AMM are thought to be similar to those responsible for the seasonal cycle in the tropical Atlantic, it is possible that wind-driven upwelling and turbulent mixing play a role in the seasonal development of the AMM (e.g., Foltz et al. 2012). Wind-induced upwelling may act concurrently with wind–evaporation–SST feedback, which is strongest in the northwestern tropical Atlantic (Chang et al. 2001), to increase the month-to-month persistence of the AMM. Numerical modeling experiments will be useful for exploring this possible mechanism.

Acknowledgments. The authors received support from the NOAA Climate Program Office and the Atlantic Oceanographic and Meteorological Laboratory. We thank two anonymous reviewers and Guy Caniaux for suggestions that improved the manuscript. The Argo data used here were collected and are made freely available by the International Argo Program and by the national programs that contribute to it. The PIRATA data used in this study were collected, processed, and made freely available by the TAO Project Office of NOAA/PMEL.

APPENDIX

Error Estimates

Here we describe the methodology used to estimate errors for each term in the mixed layer heat balance equation (1) for the analysis using satellite, Argo, and reanalysis data. Errors in mixed layer depth are estimated as one standard error of the monthly mean mixed

layer depth for each calendar month during 2001–11 and are typically ± 5 m. Errors in monthly climatological SST are $\pm 0.1^\circ\text{C}$, based on the monthly rms difference between TMI and PIRATA SST at the 4°, 12°, and 20.5°N mooring locations and assuming that the errors are uncorrelated from year to year for a given calendar month. Errors for the monthly climatological heat storage rate are calculated using standard error propagation and are about $\pm 5 \text{ W m}^{-2}$.

Similarly, uncertainties in horizontal velocity are estimated as the monthly rms difference between OSCAR and PIRATA currents at the 4°, 11.5°, and 20.5°N mooring locations. Errors were found to be $\pm 10 \text{ cm s}^{-1}$ at 4°N, $\pm 7 \text{ cm s}^{-1}$ at 11.5°N, and $\pm 7 \text{ cm s}^{-1}$ at 20.5°N for the zonal component of velocity and $\pm 8 \text{ cm s}^{-1}$ at 4°N, $\pm 6 \text{ cm s}^{-1}$ at 11.5°N, and $\pm 6 \text{ cm s}^{-1}$ at 20.5°N for the meridional component. For simplicity, we therefore assume errors in the zonal and meridional components of velocity of ± 8 and $\pm 7 \text{ cm s}^{-1}$, respectively, everywhere in the NETA region. Because of significant seasonally dependent biases present in the OSCAR currents, these errors are also used for the monthly climatological velocity errors without any reduction for temporal averaging. Errors for the monthly climatological heat storage rate are calculated using standard error propagation and are about $\pm 20 \text{ W m}^{-2}$.

Errors in 5-day averaged TropFlux surface heat fluxes were found to be $\pm 20 \text{ W m}^{-2}$ for LHF and SWR, $\pm 5 \text{ W m}^{-2}$ for LWR, and $\pm 2 \text{ W m}^{-2}$ for SHF (Kumar et al. 2012). It is assumed that the errors are uncorrelated in time so that they are reduced by $\sqrt{6}/6$ when averaging to monthly means. Because there may be significant seasonally dependent biases in the surface heat fluxes, the errors for monthly climatological values are assumed to equal the monthly errors (i.e., $\pm 8 \text{ W m}^{-2}$ for LHF and SWR, $\pm 2 \text{ W m}^{-2}$ for LWR, and $\pm 1 \text{ W m}^{-2}$ for SHF).

The uncertainties described above represent the errors associated with uneven temporal and spatial sampling from Argo and satellite sensors, combined with uncertainties in the algorithms used to calculate surface fluxes in TropFlux and horizontal currents in OSCAR. These errors are referred to as data errors (e_{data}). Total errors for the monthly-mean climatologies of each term in (1) can then be expressed as $e_{\text{tot}} = \sqrt{e_{\text{data}}^2 + e_{\text{seas}}^2}$, where e_{seas} is the error that results from calculating a seasonal cycle with a finite data length. We calculate e_{seas} as one standard error for each calendar month for each term in (1). It is found that e_{tot} is dominated by data errors because of the dominance of the seasonal cycle in the NETA region. Errors in the residual term in (1) are calculated from the errors in the other terms in (1) using standard error propagation and are typically $\pm 25 \text{ W m}^{-2}$.

REFERENCES

- Balaguru, K., P. Chang, R. Saravanan, and C. J. Jang, 2012: Barrier layers of the Atlantic warm pool: Formation mechanism and influence on the mean climate. *Tellus*, **64**, 18162–18179, doi:10.3402/tellusa.v64i0.18162.
- Bates, S. C., 2010: Seasonal influences on coupled ocean–atmosphere variability in the tropical Atlantic Ocean. *J. Climate*, **23**, 582–604.
- Bonjean, F., and G. S. E. Lagerloef, 2002: Diagnostic model and analysis of the surface currents in the tropical Pacific Ocean. *J. Phys. Oceanogr.*, **32**, 2938–2954.
- Bourlès, B., and Coauthors, 2008: The PIRATA program: History, accomplishments, and future directions. *Bull. Amer. Meteor. Soc.*, **89**, 1111–1125.
- Brandt, P., F. A. Schott, C. Provost, A. Kartavtseff, V. Hormann, B. Bourlès, and J. Fischer, 2006: Circulation in the central equatorial Atlantic: Mean and intraseasonal to seasonal variability. *Geophys. Res. Lett.*, **33**, L07609, doi:10.1029/2005GL025498.
- Caniaux, G., H. Giordani, J. L. Redelsperger, F. Guichard, E. Key, and M. Wade, 2011: Coupling between the Atlantic cold tongue and the West African monsoon in boreal spring and summer. *J. Geophys. Res.*, **116**, C04003, doi:10.1029/2010JC006570.
- Carton, J. A., and B. H. Huang, 1994: Warm events in the tropical Atlantic. *J. Phys. Oceanogr.*, **24**, 888–903.
- , and Z. X. Zhou, 1997: Annual cycle of sea surface temperature in the tropical Atlantic Ocean. *J. Geophys. Res.*, **102** (C13), 27813–27824.
- Chang, P., and S. G. Philander, 1994: A coupled ocean–atmosphere instability of relevance to the seasonal cycle. *J. Atmos. Sci.*, **51**, 3627–3648.
- , L. Ji, and H. Li, 1997: A decadal climate variation in the tropical Atlantic Ocean from thermodynamic air–sea interactions. *Nature*, **385**, 516–518.
- , —, and R. Saravanan, 2001: A hybrid coupled model study of tropical Atlantic variability. *J. Climate*, **14**, 361–390.
- Chiang, J. C. H., and D. J. Vimont, 2004: Analogous Pacific and Atlantic meridional modes of tropical atmosphere–ocean variability. *J. Climate*, **17**, 4143–4158.
- , Y. Kushnir, and A. Giannini, 2002: Deconstructing Atlantic intertropical convergence zone variability: Influence of the local cross-equatorial sea surface temperature gradient and remote forcing from the eastern equatorial Pacific. *J. Geophys. Res.*, **107**, 4004, doi:10.1029/2000JD000307.
- Czaja, A., P. Van der Vaart, and J. Marshall, 2002: A diagnostic study of the role of remote forcing in tropical Atlantic variability. *J. Climate*, **15**, 3280–3290.
- Doi, T., T. Tozuka, and T. Yamagata, 2010: The Atlantic meridional mode and its coupled variability with the Guinea Dome. *J. Climate*, **23**, 455–475.
- , G. A. Vecchi, A. J. Rosati, and T. L. Delworth, 2012: Biases in the Atlantic ITCZ in seasonal–interannual variations for a coarse- and a high-resolution coupled climate model. *J. Climate*, **25**, 5494–5511.
- Fairall, C. W., E. F. Bradley, J. E. Hare, A. A. Grachev, and J. B. Edson, 2003: Bulk parameterization of air–sea fluxes: Updates and verification for the COARE algorithm. *J. Climate*, **16**, 571–591.
- Foltz, G. R., and M. J. McPhaden, 2009: Impact of barrier layer thickness on SST in the central tropical North Atlantic. *J. Climate*, **22**, 285–299.
- , S. A. Grodsky, J. A. Carton, and M. J. McPhaden, 2003: Seasonal mixed layer heat budget of the tropical Atlantic Ocean. *J. Geophys. Res.*, **108**, 3146, doi:10.1029/2002JC001584.
- , J. Vialard, B. P. Kumar, and M. J. McPhaden, 2010: Seasonal mixed layer heat balance of the southwestern tropical Indian Ocean. *J. Climate*, **23**, 947–965.
- , M. J. McPhaden, and R. Lumpkin, 2012: A strong Atlantic meridional mode event in 2009: The role of mixed layer dynamics. *J. Climate*, **25**, 363–380.
- , A. T. Evan, H. P. Freitag, S. Brown, and M. J. McPhaden, 2013: Dust accumulation biases in PIRATA shortwave radiation records. *J. Atmos. Oceanic Technol.*, **30**, 1414–1432.
- Giordani, H., G. Caniaux, and A. Voltaire, 2013: Intraseasonal mixed layer heat budget in the equatorial Atlantic during the cold tongue development in 2006. *J. Geophys. Res.*, **118**, 650–671, doi:10.1029/2012JC008280.
- Gregg, M. C., T. B. Sanford, and D. P. Winkel, 2003: Reduced mixing from the breaking of internal waves in equatorial waters. *Nature*, **422**, 513–515.
- Grodsky, S. A., J. A. Carton, C. Provost, J. Servain, J. A. Lorenzetti, and M. J. McPhaden, 2005: Tropical instability waves at 0°N, 23°W in the Atlantic: A case study using Pilot Research Moored Array in the Tropical Atlantic (PIRATA) mooring data. *J. Geophys. Res.*, **110**, C08010, doi:10.1029/2005JC002941.
- Hayes, S. P., P. Chang, and M. J. McPhaden, 1991: Variability of the sea surface temperature in the eastern equatorial Pacific during 1986–88. *J. Geophys. Res.*, **96** (C8), 10553–10566.
- Hummel, R., M. Dengler, and B. Bourlès, 2013: Seasonal and regional variability of upper ocean diapycnal heat flux in the Atlantic cold tongue. *Prog. Oceanogr.*, **111**, 52–74, doi:10.1016/j.pocean.2012.11.001.
- Jouanno, J., F. Marin, Y. du Penhoat, J. Sheinbaum, and J. M. Molines, 2011: Seasonal heat balance in the upper 100 m of the equatorial Atlantic Ocean. *J. Geophys. Res.*, **116**, C09003, doi:10.1029/2010JC006912.
- Kalnay, E., and Coauthors, 1996: The NCEP/NCAR 40-Year Reanalysis Project. *Bull. Amer. Meteor. Soc.*, **77**, 437–471.
- Kaufman, Y. J., I. Koren, L. A. Remer, D. Tanr, P. Ginoux, and S. Fan, 2005: Dust transport and deposition observed from the Terra-Moderate Resolution Imaging Spectroradiometer (MODIS) spacecraft over the Atlantic Ocean. *J. Geophys. Res.*, **110**, D10S12, doi:10.1029/2003JD004436.
- Keenlyside, N. S., and M. Latif, 2007: Understanding equatorial Atlantic interannual variability. *J. Climate*, **20**, 131–142.
- Klein, S. A., and D. L. Hartmann, 1993: The seasonal cycle of low stratiform clouds. *J. Climate*, **6**, 1587–1606.
- Kraus, E. B., and J. S. Turner, 1967: A one-dimensional model of the seasonal thermocline. *Tellus*, **19**, 98–105.
- Kumar, B. P., J. Vialard, M. Lengaigne, V. S. N. Murty, and M. J. McPhaden, 2012: TropFlux: Air–sea fluxes for the global tropical oceans—Description and evaluation. *Climate Dyn.*, **38**, 1521–1543, doi:10.1007/s00382-011-1115-0.
- Lumpkin, R., and G. J. Johnson, 2013: Global ocean surface velocities from drifters: Mean, variance, ENSO response, and seasonal cycle. *J. Geophys. Res.*, **118**, 2992–3006, doi:10.1002/jgrc.20210.
- McClain, C. R., and J. Firestone, 1993: An investigation of Ekman upwelling in the North Atlantic. *J. Geophys. Res.*, **98** (C7), 12327–12339.
- Mignot, J., A. Lazar, and M. Lacarra, 2012: On the formation of barrier layers and associated vertical temperature inversions: A focus on the northwestern tropical Atlantic. *J. Geophys. Res.*, **117**, C02010, doi:10.1029/2011JC007435.

- Mitchell, T. P., and J. M. Wallace, 1992: The annual cycle in equatorial convection and sea surface temperature. *J. Climate*, **5**, 1140–1156.
- Moisan, J. R., and P. P. Niiler, 1998: The seasonal heat budget of the North Pacific: Net heat flux and heat storage rates (1950–1990). *J. Phys. Oceanogr.*, **28**, 401–421.
- Morel, A., and D. Antoine, 1994: Heating rate within the upper ocean in relation to its biooptical state. *J. Phys. Oceanogr.*, **24**, 1652–1665.
- Muñoz, E., W. Weijer, S. A. Grodsky, S. C. Bates, and I. Wainer, 2012: Mean and variability of the tropical Atlantic Ocean in the CCSM4. *J. Climate*, **25**, 4860–4882.
- Niiler, P. P., and E. B. Kraus, 1977: One-dimensional models of the upper ocean. *Modelling and Prediction of the Upper Layers of the Ocean*, E. B. Kraus, Ed., Pergamon, 143–172.
- Nobre, C., and J. Shukla, 1996: Variation of sea surface temperature, wind stress, and rainfall over the tropical Atlantic and South America. *J. Climate*, **9**, 2464–2479.
- Owens, W. B., and A. P. S. Wong, 2009: An improved calibration method for the drift of the conductivity sensor on autonomous CTD profiling floats by theta-S climatology. *Deep-Sea Res. I*, **56**, 450–457.
- Pailler, K., B. Bourles, and Y. Gouriou, 1999: The barrier layer in the western tropical Atlantic Ocean. *Geophys. Res. Lett.*, **26**, 2069–2072.
- Payne, R. E., 1972: Albedo of the sea surface. *J. Atmos. Sci.*, **29**, 959–970.
- Peter, A. C., M. Le Henaff, Y. Du Penhoat, C. E. Menkes, F. Marin, J. Vialard, G. Caniaux, and A. Lazar, 2006: A model study of the seasonal mixed layer heat budget in the equatorial Atlantic. *J. Geophys. Res.*, **111**, C06014, doi:10.1029/2005JC003157.
- Rienecker, M. M., and Coauthors, 2011: MERRA: NASA's Modern-Era Retrospective Analysis for Research and Applications. *J. Climate*, **24**, 3624–3648.
- Siedler, G., N. Zangenberg, and R. Onken, 1992: Seasonal changes in the tropical Atlantic circulation: Observation and simulation of the Guinea Dome. *J. Geophys. Res.*, **97** (C1), 703–715.
- Stramma, L., S. Hüttl, and J. Schafstall, 2005: Water masses and currents in the upper tropical northeast Atlantic off northwest Africa. *J. Geophys. Res.*, **110**, C12006, doi:10.1029/2005JC002939.
- Sweeney, C., A. Gnanadesikan, S. M. Griffies, M. J. Harrison, A. J. Rosati, and B. L. Samuels, 2005: Impacts of shortwave penetration depth on large-scale ocean circulation and heat transport. *J. Phys. Oceanogr.*, **35**, 1103–1119.
- Tanguy, Y., S. Arnault, and P. Lattes, 2010: Isothermal, mixed, and barrier layers in the subtropical and tropical Atlantic Ocean during the ARAMIS experiment. *Deep-Sea Res. I*, **57**, 501–517.
- Wang, W. M., and M. J. McPhaden, 1999: The surface-layer heat balance in the equatorial Pacific Ocean. Part I: Mean seasonal cycle. *J. Phys. Oceanogr.*, **29**, 1812–1831.
- Xie, S.-P., and S. G. H. Philander, 1994: A coupled ocean-atmosphere model of relevance to the ITCZ in the eastern Pacific. *Tellus*, **46**, 340–350.
- Yamagata, T., and S. Iizuka, 1995: Simulation of the tropical thermal domes in the Atlantic: A seasonal cycle. *J. Phys. Oceanogr.*, **25**, 2129–2140.
- Yu, L. S., X. Z. Jin, and R. A. Weller, 2006: Role of net surface heat flux in seasonal variations of sea surface temperature in the tropical Atlantic Ocean. *J. Climate*, **19**, 6153–6169.
- Zebiak, S. E., 1993: Air–sea interaction in the equatorial Atlantic region. *J. Climate*, **6**, 1567–1586.
- Zhang, Y., W. B. Rossow, A. A. Lacis, V. Oinas, and M. I. Mishchenko, 2004: Calculation of radiative fluxes from the surface to top of atmosphere based on ISCCP and other global data sets: Refinements of the radiative transfer model and the input data. *J. Geophys. Res.*, **109**, D19105, doi:10.1029/2003JD004457.
- Zhu, J., B. Huang, and M. A. Balmaseda, 2012: An ensemble estimation of the variability of upper-ocean heat content over the tropical Atlantic Ocean with multi-ocean reanalysis products. *Climate Dyn.*, **39**, 1001–1020.